JOURNAL OF COMPUTATIONAL PHYSICS 66, 197–217 (1986)

A Relativistic Multiregion Bounce-Averaged Fokker–Planck Code for Mirror Plasmas

Y. MATSUDA AND J. J. STEWART

Lawrence Livermore National Laboratory,
University of California, Livermore, California 94550

Received April 26, 1985; revised January 30, 1986

We have developed a unique Fokker–Planck code to study the physics of plasmas that are trapped in magnetic and potential wells of general shape on a collisional time scale. The code was designed primarily to apply to mirror machines, either a simple mirror or a tandem mirror. A plasma confined in a mirror machine generally consists of various groups of particles trapped magnetically and/or electrostatically depending on their energy, magnetic moment, and axial position. Characteristic features of such a plasma are: first, that the bounce times of trapped particles are much shorter than the collision times; and second, that particles trapped in different axial locations can have the same energy and magnetic moment. The former feature allows us to perform bounce-orbit averaging of the kinetic equation, and the latter feature indicates that the distribution function can be multivalued. The code solves a relativistic Fokker–Planck equation averaged over bounce orbits for all the trapped-particle groups. In addition to the Coulomb collision operator, the code includes a synchrotron radiation term, a quasilinear rf diffusion operator, and source and loss terms. The numerical method consists of a mapping technique and a Galerkin finite-element method. Example results using the code for electron-cyclotron resonant heating and neutral beam injection in a tandem mirror are also presented.

1. INTRODUCTION

The numerical solutions to a Fokker–Planck equation describing collisional processes in a plasma provide us with quantitative information on plasma behavior (e.g., particle and energy confinement times); thus, they have become an essential tool for understanding confinement experiments and for designing larger devices and reactors. Many Fokker–Planck studies have been done in areas such as confinement in a magnetic mirror, neutral beam injection in a mirror and a tokamak, lower-hybrid current drive, runaway electrons, and ion-cyclotron resonant heating. Killeen and his colleagues [1, 2] have made many contributions to these Fokker–Planck studies; both in the one- and two-dimensional velocity space and in the single- and multi-species cases. Most of these Fokker–Planck studies, however, used a square-well model where the magnetic field and potential profiles in the axial direction are approximated by a square-well shape with a certain mirror ratio. Thus, no spatial variation is involved and the Fokker–Planck equation is solved in one- or two-dimensional velocity space.

0021-9991/86 $3.00

One method of including the axial variation of a plasma trapped in a magnetic/potential well is the bounce-averaging technique. This technique is based on an assumption that the bounce time is much shorter than the collision time for a representative trapped particle. This technique allows us to include the effects of axial variation without extending the calculation into three dimensions; the equation is still solved in a two-dimensional phase space. An early Fokker–Planck code employing bounce averaging was written by Cutler, Pearlstein, and Rensink [3] and was used to study mirror confinement of ions. It solves a nonlinear, non-relativistic Fokker–Planck equation for ions using a finite difference method. Fyfe and Bernstein [4] developed a bounce-averaged code with a linearized non-relativistic Fokker–Planck operator to study particle losses from a deep electrostatic-magnetic well; they employ a finite-element method. Recently a bounce-averaged code was developed to study tokamak transport problems by Kerbel and McCoy [5]. It uses a finite difference method for a Fokker–Planck operator. Their code is capable of solving for a passing particle distribution as well as a trapped particle distribution and includes a detailed treatment of rf heating. Note that bounce-averaged calculations often show a significant quantitative difference from square-well calculations; and this is of great practical importance in designing large experimental devices and fusion reactors.

Another aspect of all the Fokker–Planck codes developed so far is that they can treat only a single group of trapped particles. In a mirror machine with more than one magnetic well and/or with electrostatic potential, several groups of trapped particles exist that interact with each other through Coulomb collisions. In such situations, more than one particle occurs with the same energy and magnetic moment, and these particles are separated in space. This means that to solve a typical problem for a mirror machine, we must deal with a multivalued distribution function. To illustrate this, we consider electrons trapped in a mirror system (Fig. 1). The magnetic field B has a single well and the potential Φ has a dip and a

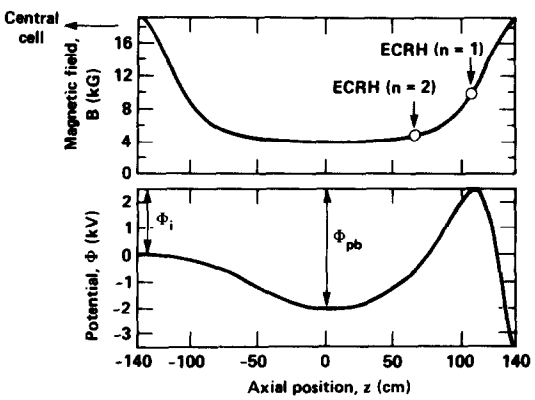

FIG. 1. Magnetic field and potential profiles in the end plug of a tandem mirror. The central cell is to the left, and the end wall is to the right.

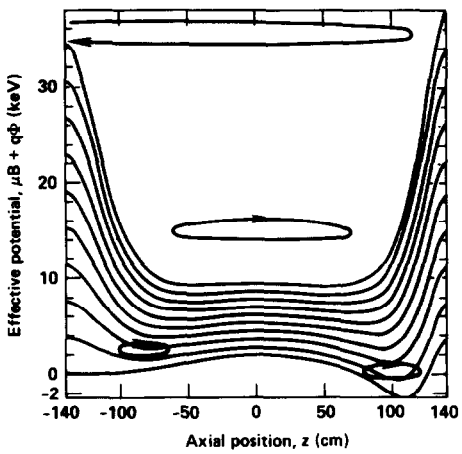

FIG. 2. Effective potential as a function of the axial position with magnetic moment as a parameter. This illustrates three groups of trapped electrons and a group of passing electrons from the central cell.

peak; this represents a typical end-plug configuration for a tandem mirror with thermal barriers [6]. The dip in the potential is usually referred to as a thermal barrier; and the peak is often referred to as a plug potential.

It is informative to plot the effective potential for parallel motion of an electron as a function of axial position, z. In Fig. 2, we plot $\mu B(z) + q\Phi(z)$, which is the effective potential in a nonrelativistic case, with magnetic moment μ as a parameter, where $q[=Ze]$ is the particle charge. We see that for a given μ and a certain range of total energy ε, two spatially separated trapped electrons can exist. This fact is also represented in the electron phase-space diagram shown in Fig. 3; i.e., the part

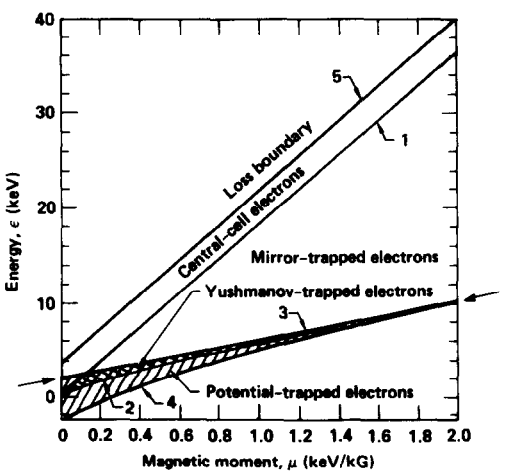

FIG. 3. Phase-space diagram for electrons in the end plug illustrated in Fig. 1. The arrows indicate the interface below which the phase-space consists of two planes.

of the phase-space below boundary 3 consists of two planes. Figure 3 is an example of a three-region problem: the first region being limited by boundaries 1 and 3, the second by boundaries 1, 2, and 3, the third by boundaries 3 and 4. A "region" refers to that part of the phase-space associated with a group of trapped particles.

In this article, we describe a relativistic Fokker–Planck code developed to solve a Fokker–Planck equation in a phase space such as shown in Fig. 3, and we will present some numerical results from a few example problems. In Section 2, we present the relativistic bounce-averaged Fokker–Planck equation derived by Bernstein and Baxter [7], and we discuss boundary conditions. In Section 3, we describe the numerical method based on a mapping technique and a Galerkin finite-element procedure, which contrasts with the finite difference method employed in most existing Fokker–Planck codes. We then present our example calculations and the results in Section 4, and our conclusions in Section 5.

2. Relativistic Bounce-Averaged Fokker–Planck Equation

The Fokker–Planck kinetic equation for a distribution function f can be written as

$$\frac{\partial f}{\partial t}+\mathbf{v}\cdot\frac{\partial f}{\partial \mathbf{x}}+\frac{\partial}{\partial \mathbf{p}}\cdot\left[q\left(\mathbf{E}+\frac{1}{c}\mathbf{v}\times\mathbf{B}\right)f+\mathbf{\Gamma}_c+\mathbf{\Gamma}_R\right]=0, \tag{1}$$

where t is the time, $\mathbf{v}$ is the velocity, $\mathbf{x}$ is the position, m is the mass, $\mathbf{p}$ $[=\gamma m\mathbf{v}]$ is the momentum, γ $[=(1+p^2/m^2c^2)^{1/2}=(1-v^2/c^2)^{-1/2}]$ is the relativistic factor, c is the speed of light, and $\mathbf{E}$ and $\mathbf{B}$ are electric and magnetic fields including both static and rf components. The flux $\mathbf{\Gamma}_c$ due to small-angle Coulomb collisions is given by

$$\mathbf{\Gamma}_c=-\sum_b\frac{2\pi Z^2Z_b^2e^4\ln\Lambda_b}{m_b^3}\int d^3\mathbf{p}_b\left(f_b\frac{\partial f}{\partial \mathbf{p}}-f\frac{\partial f_b}{\partial \mathbf{p}_b}\right)\cdot\mathbf{M}, \tag{2}$$

where subscript b refers to the particle species, and $\mathbf{M}$ is the relativistic counterpart of the dyadic $\nabla_v\nabla_v|v-v'|$ [7]. The flux $\mathbf{\Gamma}_R$ represents the radiation reaction resulted from synchrotron radiation, which is given by

$$\mathbf{\Gamma}_R=-\frac{2}{3}\frac{e^2\Omega^2\gamma_0^2}{c^3m\gamma}\left[\hat{b}\times(\mathbf{p}\times\hat{b})+\frac{1}{m^2\gamma_0^2c^2}(\hat{b}\times\mathbf{p})^2(\hat{b}\cdot\mathbf{p})\,\hat{b}\right]f, \tag{3}$$

where $\hat{b}=\mathbf{B}_0/B_0$, $\Omega=eB_0/mc$, $\gamma_0=(1+p_\perp^2/m^2c^2)^{1/2}$, and $\mathbf{B}_0$ is the static magnetic field.

Applying bounce-average theory [3, 7] to Eq. (1) yields

$$\tau\frac{\partial f}{\partial t}=\frac{\partial}{\partial\varepsilon}\left(D_{\varepsilon\varepsilon}\frac{\partial f}{\partial\varepsilon}+D_{\varepsilon\mu}\frac{\partial f}{\partial\mu}+D_\varepsilon f\right)+\frac{\partial}{\partial\mu}\left(D_{\mu\varepsilon}\frac{\partial f}{\partial\varepsilon}+D_{\mu\mu}\frac{\partial f}{\partial\mu}+D_\mu f\right), \tag{4}$$

where ε $[=mc^2(\gamma-1)+q\Phi]$ is the total energy, μ $[=p_\perp^2/2mB_0]$ is the magnetic moment, and τ $[=\oint dz/|v_\parallel|]$ is the bounce time. In Eq. (4) the coefficients on the right-hand side represent integrals of the local coefficients along the bounce orbit of a particle with a given ε and μ. Each coefficient consists of three terms: the first is the Fokker–Planck coefficient resulting from Coulomb collisions; the second is the radiation reaction term; and the last is the quasilinear rf diffusion term. We employ numerical integration along the orbit for the Coulomb collision and the radiation terms; and we use the analytical result for the rf diffusion terms obtained by Bernstein and Baxter [7].

For the Coulomb collision and radiation reaction terms, the coefficients in Eq. (4) can be written as

$$\begin{aligned}
D_{\varepsilon\varepsilon} &= \oint \frac{dz}{v_\parallel m^2\gamma^2}\,\mathbf{p}\cdot\mathbf{D}\cdot\mathbf{p},\\
D_{\varepsilon\mu} &= \oint \frac{dz}{v_\parallel m^2\gamma B_0}\,\mathbf{p}\cdot\mathbf{D}\cdot\mathbf{p}_\perp,\\
D_{\varepsilon} &= \oint \frac{dz}{v_\parallel m\gamma}\,\mathbf{p}\cdot\mathbf{A},\\
D_{\mu\varepsilon} &= \oint \frac{dz}{v_\parallel m^2\gamma B_0}\,\mathbf{p}_\perp\cdot\mathbf{D}\cdot\mathbf{p},\\
D_{\mu\mu} &= \oint \frac{dz}{v_\parallel m^2 B_0^2}\,\mathbf{p}_\perp\cdot\mathbf{D}\cdot\mathbf{p}_\perp,\\
D_{\mu} &= \oint \frac{dz}{v_\parallel mB_0}\,\mathbf{p}_\perp\cdot\mathbf{A},
\end{aligned} \tag{5}$$

where $\mathbf{D}$ and $\mathbf{A}$ are the coefficients of the local kinetic equation expressed in the form

$$\frac{\partial f}{\partial t} = \frac{\partial}{\partial \mathbf{p}}\cdot\left(\mathbf{D}\cdot\frac{\partial f}{\partial \mathbf{p}} + \mathbf{A}f\right). \tag{6}$$

The local coefficients $\mathbf{D}$ and $\mathbf{A}$ due to Coulomb collisions are given by

$$\begin{aligned}
\mathbf{D}^c &= m^2\nabla_v\nabla_v G,\\
\mathbf{A}^c &= -m\nabla_v H,\\
H &= \sum_b \frac{4\pi Z^2 Z_b^2 e^4 \ln\Lambda_b}{mm_b}\,h_b, \qquad \nabla_v^2 h_b = -4\pi f_b,\\
G &= \sum_b \frac{2\pi Z^2 Z_b^2 e^4 \ln\Lambda_b}{m^2}\,g_b, \qquad \nabla_v^2 g_b = 2h_b,
\end{aligned} \tag{7}$$

for nonrelativistic particles, and

$$\mathbf{D}^c = \sum_b 2\pi n_b m Z^2 Z_b^2 e^4 \ln \Lambda_b \left\{ \gamma \frac{p^2 \mathbf{I} - \mathbf{pp}}{p^3} + \frac{2\gamma^3 m^2 \langle u_b^2 \rangle}{3p^5} \mathbf{pp} \right\},$$

$$\mathbf{A}^c = \sum_b 2\pi n_b m Z^2 Z_b^2 e^4 \ln \Lambda_b \frac{2\gamma^2 m \mathbf{p}}{m_b p^3}, \tag{8}$$

$$\langle u_b^2 \rangle = \frac{2\bar{E}_b}{m_b},$$

for relativistic particles [7]. Here $\bar{E}_b$ is the average kinetic energy of particle species b, $\ln \Lambda_b$ is the coulomb logarithm; and I is the unit dyadic. We employ the nonlinear, nonrelativistic collision operator, Eq. (7), below a certain energy and the linear relativistic operator, Eq. (8), above that energy. Because of the diffusive nature of the equation we do not expect a great sensitivity to a small discontinuity of the diffusion coefficients at this energy. This is, of course, a simple approximation to fully nonlinear relativistic collision operator. However, it is a good approximation if a distribution consists of a nonrelativistic bulk and a small population of a high energy tail.

The terms **D** and **A** resulting from the synchrotron radiation are given by [7],

$$\mathbf{D}^R = 0,$$

$$\mathbf{A}^R = \frac{2}{3} \frac{e^2 \Omega^2 \gamma_0^2}{c^3 \gamma m} \left[\hat{b} \times (\mathbf{p} \times \hat{b}) + \frac{(\hat{b} \times \mathbf{p})^2}{m^2 \gamma_0^2 c^2} (\hat{b} \cdot \mathbf{p}) \hat{b} \right]. \tag{9}$$

For the rf diffusion, the coefficients on the right-hand side of Eq. (4) are given by

$$D_{\varepsilon\varepsilon} = \sum_n \sum_j |I_j|^2 \left| \frac{e\mathbf{a}_j \cdot \mathbf{V}_j}{2\gamma_j} \right|^2,$$

$$D_{\varepsilon\mu} = D_{\mu\varepsilon} = \sum_n \sum_j \frac{|I_j|^2}{2} \left\{ \frac{e\mathbf{a}_j^*}{2\gamma_j} \cdot \mathbf{V}_j^* \frac{e}{2B_{0j}} \left[\mathbf{a}_j + \frac{u_j \hat{b} \times (\mathbf{k} \times \mathbf{a}_j)}{\omega \gamma_j} \right] \cdot \mathbf{W}_j \right\} + \text{c.c.},$$

$$D_{\mu\mu} = \sum_n \sum_j |I_j|^2 \left| \frac{e}{2B_{0j}} \left[\mathbf{a}_j + \frac{u_j \hat{b} \times (\mathbf{k} \times \mathbf{a}_j)}{\omega \gamma_j} \right] \cdot \mathbf{W}_j \right|^2,$$

$$D_\varepsilon = D_\mu = 0,$$

$$\mathbf{V}_j = u_j \hat{b} J_n(k_\perp \rho_j) + \mathbf{W}_j,$$

$$\mathbf{W}_j = \tfrac{1}{2} w_j [(\hat{e}_1 - i\hat{e}_2) J_{n-1}(k_\perp \rho_j) e^{i\theta} + (\hat{e}_1 + i\hat{e}_2) J_{n+1}(k_\perp \rho_j) e^{-i\theta}] \tag{10}$$

$$|I_j|^2 = \begin{cases} 2\pi/|\dot{v}_j| & \text{for } x \gg 1 \\ (2\pi)^2 (\ddot{v}_j/2)^{-2/3} Ai^2(-x) & \text{for } x < 1, \end{cases}$$

$$v = \frac{n\Omega}{\gamma} - \omega + k_{\parallel} v_{\parallel}, \qquad \dot{v} \equiv \frac{dv}{dt}, \qquad x \equiv 2^{-2/3} \dot{v}_j^2 \ddot{v}_j^{-4/3},$$

$$\rho_j = \frac{1}{\Omega_j} \left(\frac{2\mu B_{0j}}{m} \right)^{1/2},$$

where n represents the cyclotron harmonic number, subscript j represents the stationary phase point (i.e., the resonant point satisfying $v = 0$), $\mathbf{a}_j$ is the rf electric field at the jth resonant point, u_j $[= p_{\parallel j}/m]$ and w_j $[= p_{\perp j}/m]$ are local parallel and perpendicular momentum-per-unit mass, respectively, B_{0j} is the static magnetic field, $\hat{e}_1$, $\hat{e}_2$, and $\hat{b}$ comprise a right-handed orthogonal set, $\mathbf{k}$ is the wave vector, θ is the angle between $\mathbf{k}$ and $\hat{e}_1$, ω is the rf frequency, $Ai(-x)$ is the Airy function, and $J_n(k_\perp \rho_j)$ is the nth-order Bessel function of the first kind. The resonant points satisfying $v = 0$ are numerically calculated for a given magnetic field and potential profiles.

With all the coefficients determined as above, we can solve Eq. (4) for each group of trapped particles in a phase space such as shown in Fig. 3 with appropriate boundary conditions. The necessary and sufficient boundary conditions are

(1) f regular at $v_{\parallel} = 0$ and $\mu = 0$ boundary,

(2) f fixed at loss boundary,

(3) f or flux Γ vanishing at $\varepsilon = \varepsilon_{\max}$ and/or $\mu = \mu_{\max}$,

(4) f and flux Γ continuous at interface

In Fig. 3, the boundary condition (1) at $v_{\parallel} = 0$ is applied to boundary 2 and 4; the phase-space below these boundaries is inaccessible. Condition (2) is applied to boundary 1 and the first segment of boundary 3; these boundaries separate a passing particle distribution, which is taken to be fixed, and a trapped particle distribution. Condition (4) is applied along the interface between three regions, i.e., the second segment of boundary 3. Specifically the flux continuity condition is $\Gamma_1 + \Gamma_2 + \Gamma_3 = 0$.

In the next section, we will describe a numerical method for solving Eq. (4) with the above boundary conditions.

3. Numerical Method

We employ the same method developed by Fyfe *et al.* [8] in solving Eq. (4). It consists of two steps: first, map a region in (μ, ε) phase-space to a retangular region in (x, y) space; and second, use a Galerkin finite-element method. The same procedure is also applied to solving the Poisson equation for the Rosenbluth potentials h_b and g_b.

The mapping technique is introduced to represent the curved boundary more accurately than is possible when working directly in (μ, ε), $(v_{\parallel}, v_{\perp})$, or (v, θ) space.

Having boundaries running between the grid points is usually unavoidable, unless either a mapping or a finite element method is used; this is especially a concern when a distribution function is largest along a curved boundary. In a tandem-mirror thermal barrier, ions have to be constantly pumped out at the same rate as the trapping rate to maintain the density dip. The ion distribution in this situation is peaked along the boundary between passing and trapped regions. If one solves the problem in $(v_\parallel, v_\perp)$ or (v, θ) space, for example, this boundary is curved and cannot be aligned with any grid. Since the trapping rate is directly dependent on the derivative of the distribution function on the boundary, the boundary must be represented more accurately. The mapping also allows efficient integration over finite elements because solutions are obtained in a rectangular geometry.

The Galerkin method has a convenient feature that will make implementation of boundary conditions straightforward. Especially, the Neumann condition (zero flux condition) is implemented by simply dropping a surface term in the finite element equation. The flux continuity condition at the interface can be satisfied exactly in this procedure.

Note that Eq. (4) is a nonlinear equation in f. However, in implementing the numerical procedure, we linearize Eq. (4); i.e., in calculating the coefficients, which are functionals of f, we substitute f from the previous time step.

3.1. *Mapping*

Consider a region in a two-dimensional space with coordinates (S, T) as shown in Fig. 4. The coordinates S and T are typically physical variables such as velocities, energy, and magnetic moment. The region is enclosed by two straight lines $S = S_{\min}$ and $S = S_{\max}$, and two curved lines $T = h(S)$ and $T = l(S)$, where h and l are single-valued functions of S and piecewise continuous up to at least the first derivative. The transformation is then given by

$$x = S,$$
$$y = \frac{(y_{\max} - y_{\min})\, T - [y_{\max}\, l(S) - y_{\min}\, h(S)]}{h(S) - l(S)}, \tag{11}$$

which maps the region in (S, T) space into a rectangular region,

$$x_{\min} \leqslant x \leqslant x_{\max}, \qquad y_{\min} \leqslant y \leqslant y_{\max}$$

in (x, y) space.

Using μ and ε in place of S and T the transformation Eq. (11) reduces Eq. (4) to

$$J\tau \frac{\partial f}{\partial t} = \frac{\partial}{\partial x}\left(D_{xx}\frac{\partial f}{\partial x} + D_{xy}\frac{\partial f}{\partial y} + D_x f\right) + \frac{\partial}{\partial y}\left(D_{yx}\frac{\partial f}{\partial x} + D_{yy}\frac{\partial f}{\partial y} + D_y f\right), \tag{12}$$

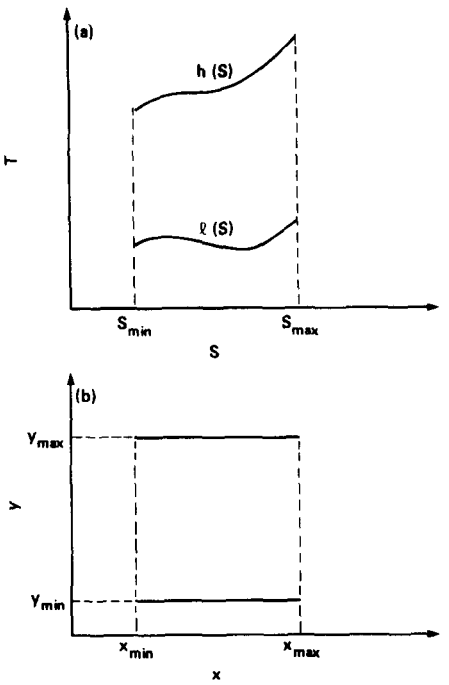

FIG. 4. Mapping from a physical space in (S, T) to a rectangular space in (x, y).

where J is the Jacobian of the transformation,

$$J=\frac{\partial\varepsilon}{\partial y}\frac{\partial\mu}{\partial x}=\frac{h(\mu)-l(\mu)}{y_{\max}-y_{\min}};$$

and the new coefficients are

$$D_{xx}=\frac{1}{J}\left(\frac{\partial\varepsilon}{\partial y}\right)^2 D_{\mu\mu},$$

$$D_{xy}=D_{yx}=\frac{1}{J}\left(-\frac{\partial\varepsilon}{\partial y}\frac{\partial\varepsilon}{\partial x}D_{\mu\mu}+\frac{\partial\varepsilon}{\partial y}D_{\mu\varepsilon}\right),$$

$$D_{yy}=\frac{1}{J}\left[\left(\frac{\partial\varepsilon}{\partial x}\right)^2 D_{\mu\mu}-2\frac{\partial\varepsilon}{\partial x}D_{\mu\varepsilon}+D_{\varepsilon\varepsilon}\right],$$

$$D_x=\frac{\partial\varepsilon}{\partial y}D_\mu,$$

$$D_y=D_\varepsilon-\frac{\partial\varepsilon}{\partial x}D_\mu.$$

A simple example of the mapping is shown in Fig. 5. The triangular region in (μ, ε) phase-space shown in Fig. 5a arises for a single magnetic well without potential. In this case the mapping transformation from Fig. 5a to Fig. 5b is

$$x = \mu, \qquad y = \frac{\varepsilon - \mu B_b}{\mu(B_M - B_b)}, \tag{13}$$

where B_b and B_M are the magnetic field at the bottom and the mirror throat, respectively, and we let $y_{min} = 0$, $y_{max} = 1$. Figure 5c illustrates the corresponding mesh in $(v_\parallel, v_\perp)$ space mapped from the uniform rectangular mesh in (x, y) space.

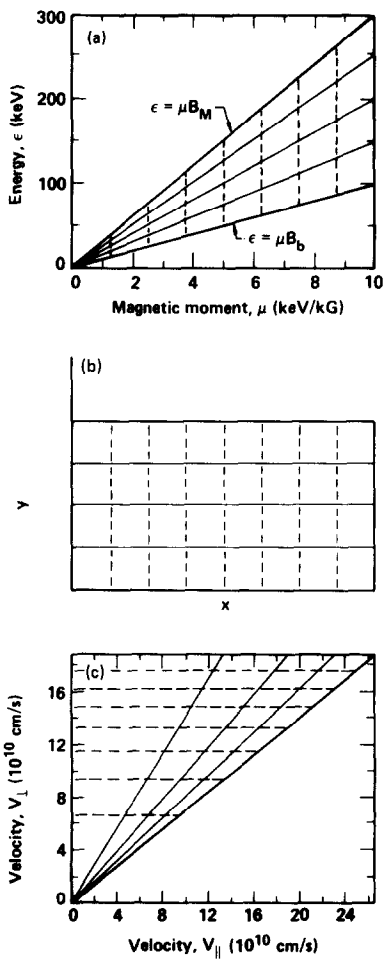

FIG. 5. (a) A phase-space diagram in (μ, ε) for a single magnetic well; also illustrated is the numerical mesh, (b) the phase-space mapped on (x, y) space with a rectangular mesh, (c) the numerical mesh in $(v_\parallel, v_\perp)$ space that corresponds to that in (b).

As a more complicated example, we consider a case of a single magnetic well with a repelling potential (Fig. 6). This is a typical situation that arises in a single mirror machine with neutral beam injection. The phase-space diagram in (ε, μ) corresponding to this case is shown in Fig. 7a. Three regions exist: one region between boundaries 1 and 3; and two regions enclosed by boundaries 1, 2, and 3. The latter two regions are on separate planes; they look identical because of the symmetry of the profiles of $B(z)$ and $q\Phi(z)$. The particles in these two regions are trapped off the midplane and never pass the midplane. We apply the mapping [Eq. (11)] to each region separately as shown schematically in Fig. 7. Figure 7 also illustrates the corresponding mesh in (μ, ε) space, which is mapped from the numerical mesh in (x, y) space. Note that the transformation for the two regions (below boundary 3) has a discontinuity in the derivative at point A. This means that we have to choose a set of basis functions that allow a discontinuity in the x derivative at point A [8].

3.2. *Galerkin Method*

In the Galerkin finite element method, an approximate solution $\hat{f}$ to Eq. (12) is represented as

$$\hat{f}(x, y, t) = \sum_{i=1}^{N} c_i(t)\, B_i(x, y), \tag{14}$$

whre $B_i(x, y)$ is the ith basis function in (x, y) space and $c_i(t)$ is the ith coefficient. The solution $\hat{f}$ is then sought, which satisfies

$$\int_{\mathscr{D}} dxdy\, J\tau \frac{\partial \hat{f}}{\partial t} B_j = \int_{\mathscr{D}} dxdy\, \nabla \cdot (\mathbf{P}\nabla \hat{f} + \mathbf{Q}\hat{f})\, B_j \qquad (j = 1, 2, \ldots, N), \tag{15}$$

where $\mathscr{D}$ denotes the mapped rectangular region corresponding to each region in (μ, ε) space, and $\nabla \cdot (\mathbf{P} \cdot \nabla \hat{f} + \mathbf{Q}\hat{f})$ represents the right-hand side of Eq. (12) with ∇

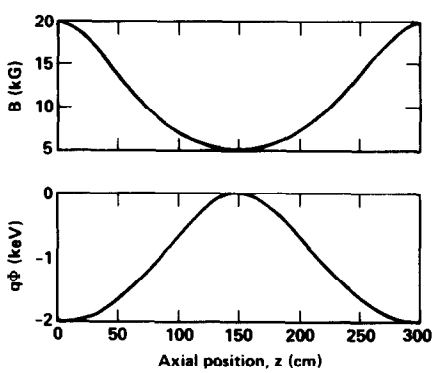

FIG. 6. Magnetic field and potential profiles of a single mirror with a repelling potential. An example of a three-region problem.

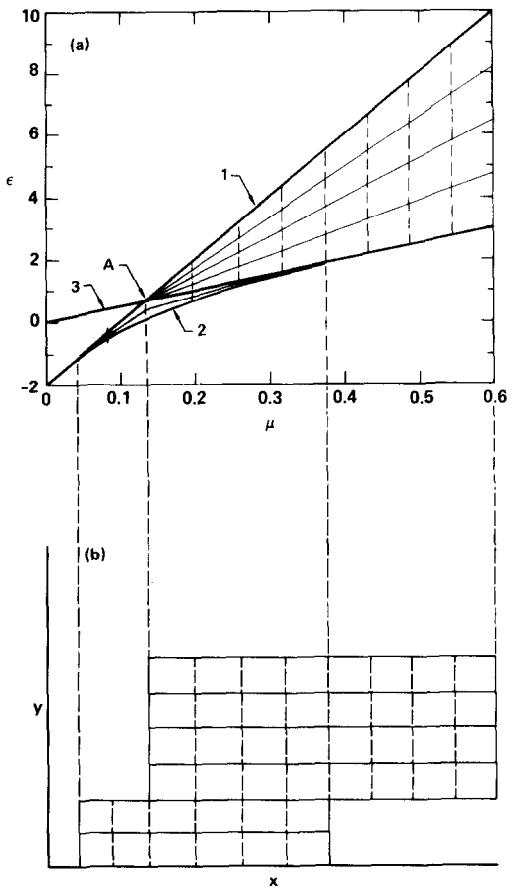

FIG. 7. (a) Phase-space diagram for the profiles shown in Fig. 6, (b) the phase-space mapped on (x, y) space with a rectangular mesh in each region.

being a gradient operator in (x, y) space. Substituting Eq. (14) into Eq. (15) and

$$\sum_{i=1}^{N}\left\{\int_{\mathscr{D}} dxdy\, J\tau B_i B_j\right\}\frac{dc_i}{dt} = -\sum_{i=1}^{N}\left\{\int_{\mathscr{D}} dxdy(\mathbf{P}\cdot\nabla B_i + \mathbf{Q}B_i)\cdot\nabla B_j\right\}c_i + (\text{surface terms}) \quad (j=1, 2,..., N) \tag{16a}$$

or in a matrix notation

$$\mathbf{B}\cdot\frac{d\mathbf{c}}{dt} = \mathbf{A}\cdot\mathbf{c} + (\text{surface terms}), \tag{16b}$$

where the elements of matrices **A** and **B** are

$$a_{ij} = \int_{\mathscr{D}} dxdy(\mathbf{P} \cdot \nabla B_i + \mathbf{Q} B_i) \cdot \nabla B_j,$$

$$b_{ij} = \int_{\mathscr{D}} dxdy\, J\tau B_i B_j.$$

Following Fyfe *et al.* [8], we chose for the basis function $B_i(x, y)$ a product of one-dimensional splines defined on a rectangular mesh, i.e.,

$$B_i(x, y) = \phi_k(x)\, \psi_l(y), \qquad i = k + N_x(l-1),$$
$$k = 1, 2, ..., k, N_x, \; l = 1, 2, ..., N_y, \tag{17}$$

where $\phi_k(x)$ and $\psi_l(y)$ are B-spline basis functions [9]. Typically we use a linear or cubic polynomial for ϕ's and ψ's. The integrals in Eq. (16), a_{ij} and b_{ij}, are computed by a Gauss quadrature rule; every integral of the form $\iint dxdy\; g(x, y)$ is approximated by

$$\int_a^b dx \int_c^d dy\; g(x, y) = \frac{b-a}{2} \cdot \frac{c-d}{2} \sum_i^{N_q} \sum_j^{N_q} w_i w_j g(\xi_i, \eta_j), \tag{18}$$

where

$$\xi_i = \frac{b-a}{2}\theta_i + \frac{b+a}{2}, \qquad \eta_j = \frac{d-c}{2}\theta_j + \frac{d+c}{2},$$

and w_i are the weights and θ_i are the nodes for the N_q-point Gaussian quadrature scheme on the interval $[-1, 1]$.

Now, let us discuss implementation of the boundary conditions. There are three types of boundary conditions to be considered; the first is the Neumann (natural) condition (or zero flux). The second is the Dirichlet condition (or fixed $\hat{f}$), and the third is the flux continuity at the interface. Equation (16) has to be modified to take into account these boundary conditions.

First, the Neumann condition is implemented simply by dropping the surface term in each equation for the coefficient c's associated with the corresponding boundary. Second, the Dirichlet condition on a certain boundary can be implemented by dropping the surface term and then modifying the elements of matrices **A** and **B** so that the coefficient c's associated with the boundary do not change in time. Finally, the flux continuity along the interface is implemented as follows. Equation (16) is a system of ordinary differential equations for the basis function coefficients c_i $(i = 1, ..., N)$; one such system is calculated for each region of the phase-space. Note that most of the surface terms are zero except for some particular i that is associated with the interface. When two equations, one from a region and the other from another region interfaced with it, are added, the surface terms

should cancel each other. The two systems of equations for the coefficients can then be combined into one with flux continuity satisfied exactly at the interface. This same procedure can be used no matter how many regions are connected at the interface. Thus, we obtain a combined system of ordinary differential equations describing the evolution of all the trapped particles,

$$\mathbf{B}^* \cdot \frac{d\mathbf{c}^*}{dt} = \mathbf{A}^* \cdot \mathbf{c}^*, \tag{19}$$

where $\mathbf{A}^*$ and $\mathbf{B}^*$ represent the combined $\mathbf{A}$ and $\mathbf{B}$ with modifications resulting from all the boundary conditions, and $\mathbf{c}^*$ is the combined basis function coefficient vector.

Time-differencing Eq. (19), we have

$$[\mathbf{B}^* \Delta t^{-1} - \beta \mathbf{A}_n^*] \cdot \mathbf{c}_{n+1}^* = [\mathbf{B}^* \Delta t^{-1} + (1-\beta)\, \mathbf{A}_n^*] \cdot \mathbf{c}_n^*, \tag{20}$$

where β is an implicitness factor and the subscript n represents the values at the nth time-step. To invert the matrix on the left-hand side of Eq. (20), we use the sparse matrix package developed at Yale University [10].

3.3. *Rosenbluth Potentials*

The Rosenbluth potentials h_b and g_b, satisfy Poisson equations as shown in Eq. (7). We chose to solve these by the Galerkin finite element method. Ignoring the gyrophase dependence, we have

$$\begin{aligned} \frac{1}{v_\perp}\frac{\partial}{\partial v_\perp}\left(v_\perp \frac{\partial h}{\partial v_\perp}\right) + \frac{\partial^2 h}{\partial v_\parallel^2} &= -4\pi f, \\ \frac{1}{v_\perp}\frac{\partial}{\partial v_\perp}\left(v_\perp \frac{\partial g}{\partial v_\perp}\right) + \frac{\partial^2 g}{\partial v_\parallel^2} &= 2h, \end{aligned} \tag{21}$$

where $v_\perp$ and $v_\parallel$ are perpendicular and parallel velocities. For simplicity we dropped the subscript b. Note that h and g are functions of axial position z, as well as $v_\perp$ and $v_\parallel$. Equation (21) is to be solved for each z-grid position. To solve Eq. (21) in a velocity space $0 \leqslant v_\perp,\ v_\parallel \leqslant v_m$, we let $S = v_\perp / v_m$, $T = v_\parallel / v_m$, and obtain

$$\begin{aligned} \frac{1}{S}\frac{\partial}{\partial S}\left(S \frac{\partial h}{\partial S}\right) + \frac{\partial^2 h}{\partial T^2} &= -4\pi v_m^2 f, \\ \frac{1}{S}\frac{\partial}{\partial S}\left(S \frac{\partial g}{\partial S}\right) + \frac{\partial^2 g}{\partial T^2} &= 2v_m^2 h. \end{aligned} \tag{22}$$

Because the velocity space is square, we can use the same finite element method without a mapping.

The boundary conditions for Eq. (22) are the following: (1) h and g are regular at

$S=0$, (2) $\partial h/\partial T=\partial g/\partial T=0$ at $T=0$, and (3) h and g are specified along $S=1$ and $T=1$, i.e., Dirichlet condition. The Dirichlet conditions are given by the following integrals:

$$h(S,T)=4v_m^2\int_0^1 dS'S'\int_0^{(1-S'^2)^{1/2}} dT'\,f(S',T')\sum_{i=1}^{2}K\left(\frac{\pi}{2},r_i\right)A_i^{-1/2},$$
$$g(S,T)=4v_m^2\int_0^1 dS'S'\int_0^{(1-S'^2)^{1/2}} dT'\,f(S',T')\sum_{i=1}^{2}E\left(\frac{\pi}{2},r_i\right)A_i^{1/2}, \tag{23}$$

where K and E are elliptic functions of the first and second kind, respectively, and

$$A_1=(S+S')^2+(T-T')^2,$$
$$A_2=(S+S')^2+(T+T')^2,$$
$$r_i=(4SS'/A_i)^{1/2}.$$

Because the diffusion coefficients $\mathbf{D}^c$ and $\mathbf{A}^c$ involve the second derivatives of h_b and g_b, we employ basis functions based on cubic B-splines to represent h_b and g_b.

4. Example Calculations

In this section, we present some numerical results of two example problems; the first is a neutral beam injection problem for a single mirror and the second is an electron-cyclotron resonant heating problem for a tandem mirror with thermal barriers. The former is an example of a single-region problem, and the latter is that of a three-region problem.

4.1. *Neutral Beam Injection*

One of the key ingredients in the operation of a tandem mirror with thermal barriers is the presence of sloshing ions in the end plugs. The sloshing ion distribution can be generated by injecting a neutral beam at an oblique angle to the magnetic field at the bottom (i.e., midplane) of a magnetic well. This creates ion density peaks off the midplane and helps establish a plug potential at one of the peaks.

To model the beam injection, we add the following term to the right-hand side of the kinetic equation

$$s=\sum_b \alpha_b(z)(\nu_i^b+\nu_x^b)\,n_i s_b(\mathbf{v})-\sum_b \alpha_b(z)\,\nu_x^b f, \tag{24}$$

where $\alpha_b(z)$ represents the axial profile of the beam; ν_i^b and ν_x^b are the ionization and charge exchange rates; n_i $[=\int d^3\mathbf{v}f]$ is the ion density; $s_b(\mathbf{v})$ is the neutral beam velocity distribution, and the superscript b denotes the bth component of the beam.

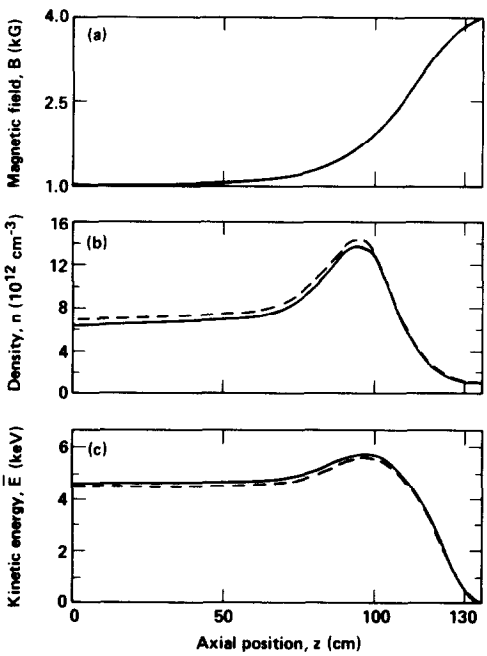

FIG. 8. (a) Magnetic field profile used for a neutral beam injection problem. The midplane is at $z = 0$. (b) Density versus axial position at the steady state; (——) result from our code, (– – –) code of Cutler *et al.* (c) Kinetic energy versus axial position at the steady state.

Equation (24) is integrated numerically along the bounce orbit and added to the right-hand side of Eq. (4). The rf diffusion and synchrotron radiation terms are not included in this calculation.

The above example was chosen to model the sloshing-ion experiment in TMX-U [11]. We calculate the end-plug ion distribution only and treat the central-cell ions as a fixed passing distribution. The magnetic field profile is shown in Fig. 8a; $z = 0$ corresponds to the midplane of the plug. The potential is ignored because the beam energy is much larger than the potential generated. Electrons are assumed to be Maxwellian with energy ($T_e = 60$ eV) smaller than the ion energy and act as drag on the ions. The neutral beam consists of three energy components; 16, 8, and 5.33 keV injected at 47° with respect to the magnetic field at $z = 0$. The effects of cold gas are also included by adding extra cold ion source and charge exchange loss. We used 48×16 mesh cells of nonuniform size, linear splines for the basis functions, 2×2 quadrature points in each cell, and 16 points in the axial direction where the Rosenbluth potentials are calculated. For the Rosenbluth potentials, we used 16×16 cells, cubic splines for the basis functions, and 4×4 quadrature points.

Figures 8b, c show the density and energy versus axial position at the steady state, and Fig. 9 shows a contour plot of the distribution function at the midplane, $z = 0$. In Fig. 8 the density and energy obtained from the code of Cutler *et al.* [3]

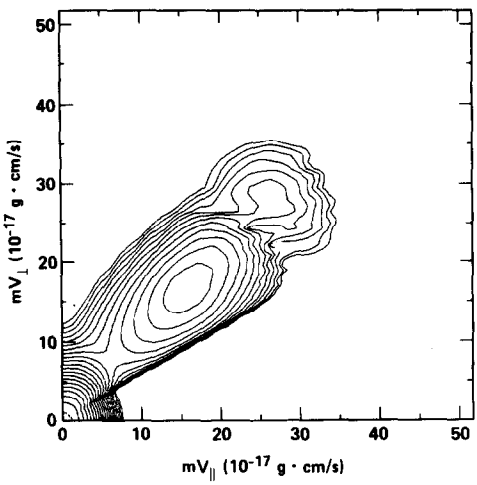

FIG. 9. Contour plot of the ion distribution function in the momentum space at the midplane that corresponds the results shown in Fig. 8.

are also shown by dashed lines. While our code uses a finite element method for both the Fokker–Planck operator and the Rosenbluth potentials, Cutler *et al.* used a finite difference method for the Fokker–Planck operator and a Legendre expansion technique in solving for the Rosenbluth potentials. These results from two different codes are in good agreement. Another different feature of the two codes is that we use energy and magnetic moment as phase-space variables while Cutler *e al.* use speed and pitch angle. Note that these Fokker–Planck code results compare favorably with a TMX-U experiment in Ref. [11].

4.2. *Electron-Cyclotron Resonant Heating*

Electron-cyclotron resonant heating (ECRH) is the other key ingredient in the operation of a tandem mirror with thermal barriers. The purpose of the ECRH is to manipulate the electron-velocity distribution in the end plugs to generate a thermal barrier and to enhance a plug potential [6]. The magnetic field and potential profiles used in this calculation are those shown in Fig. 1. The ECRH is applied at two locations: the thermal barrier and the plug potential peak. The former is to help depress the potential by generating mirror-trapped hot electrons, and the latter is to enhance the potential by heating the potential-trapped electrons.

The main objective of this three-region Fokker–Planck calculation is to find a steady-state solution for the electron distribution in the end plug. From this solution, we can obtain necessary information for operating an end plug (e.g., steady-state density and energy of the electrons, power requirement for ECRH to maintain such a steady state, and effect of wave polarization and the Doppler shift). In this example we have included relativistic kinematics although the results turned out to be only weakly relativistic; in many other applications, however, we are

interested in studying much higher energy (e.g., several hundred keV to a few MeV) electrons for which relativistic formulation is required.

We assume a fixed density and a temperature at the left mirror throat, determined by central-cell electrons with density $n_{ec} = 8 \times 10^{12}\,\mathrm{cm}^{-3}$ and temperature $T_{ec} = 0.6\,\mathrm{keV}$. These electrons determine the boundary condition and act as a source for the trapped electrons. Ions are assumed to be cold and cause pitch-angle scattering of electrons. The ECRH is applied by specifying rf electric field **a**, in Eq. (10). Fundamental heating ($\omega = \omega_{ce}$) is used at the plug potential peak ($z \simeq 110\,\mathrm{cm}$); and second harmonic heating ($\omega = 2\omega_{ce}$) is used near the bottom of the magnetic field ($z = 65\,\mathrm{cm}$). The fundamental electric field is set at 20 V/cm and has a Gaussian width of 1 cm about $z = 110\,\mathrm{cm}$. The second harmonic electric field is set at 90 V/cm with a Gaussian width of 15 cm about $z = 65\,\mathrm{cm}$. Only the right-handed circularly polarized component is used in this calculation. The synchrotron radiation term is not included. These parameters are either expected or considered reasonable to be realized in TMX-U.

The results of the Fokker–Planck calculation show that the projected density and energy of the end-plug electrons in TMX-U can be achieved with the available ECRH power [12]. The results also indicate that the plug density-potential relationship obtained from the code agrees with analysis [13]. Because the main physics results have been presented in Ref. [12], we only present part of the numerical results here. We used 32×12, 20×6, and 20×8 cells in the three regions, respectively, linear splines for the basis functions, 2×2 quadrature points in each cell, and 31 points in the axial direction, where the Rosenbluth potentials are calculated. For the Rosenbluth potential, we used 16×16 cells, cubic splines for the basis functions, and 4×4 quadrature points.

In Fig. 10a, we show the electron density and energy versus axial position obtained from the Fokker–Planck code. For comparison, the results of a Monte Carlo code are shown in Fig. 10b; the two codes are in good agreement. Figure 11 shows the electron-distribution function at steady state for three different axial

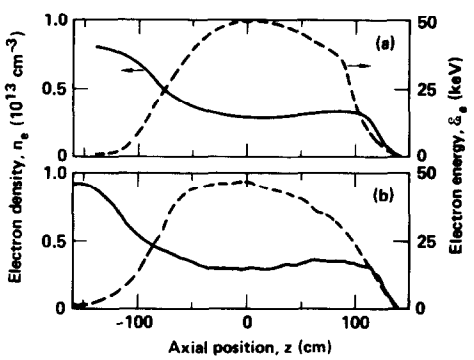

FIG. 10. Comparison of (a) our code results and (b) the Monte Carlo code result for the ECRH problem.

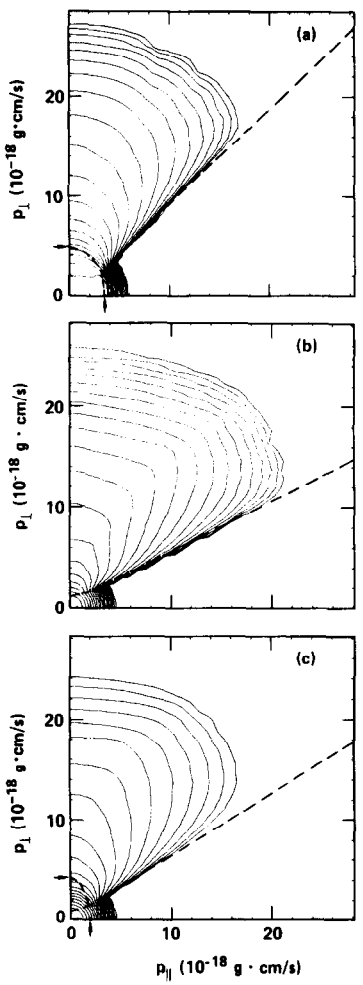

FIG. 11. Contour plot of the electron distribution function in the momentum space. The arrows indicate the interface corresponding to that in Fig. 3. (a) Near the plug potential ($z = 110$ cm). Also shown are the boundaries separating the mirror-trapped electrons, potential-trapped electrons, and the pssing electrons from the central cell. (b) At the thermal barrier ($z = 0$). The boundary shown separates the mirror-trapped electrons and the passing electrons. (c) At $z = -75$ cm. The boundaries shown separate the mirror-trapped electrons, the Yushmanov-trapped electrons, and the passing electrons.

positions: (a) near the plug potential ($z \simeq 110$ cm), (b) at the thermal barrier ($z = 0$), and (c) at a position ($z \simeq -75$ cm) between the left mirror throat and the barrier. In Fig. 11a, the elliptical region near the origin corresponds to the potetial-trapped electrons. The rf heating characteristics resulting from the ECRH fundamental heating are lines with $v_\parallel = \text{constant}$. The distribution in this region is rather flat because the rf heating dominates over collisions. The region above corresponds to the mirror-trapped hot electrons; the heating characteristics, mainly

determined by the second harmonic heating, are roughly parallel to the elliptical boundary. Figure 11b shows that the mirror-trapped distribution is pulled along the heating characteristics line that corresponds to the turning-point resonance for the second harmonic ($n=2$). The effect of the fundamental ($n=1$) heating is less obvious here than in Fig. 11a. Figure 11c shows the distribution where there exist Yushmanov-trapped electrons, which are trapped between the left mirror throat and the barrier. These electrons occupy part of the elliptical region indicated in Fig. 11c and are clearly not affected by ECRH. Note that these Yushmanov-trapped particles in general do not have a unique center of bounce motion. Therefore, a reference point for a single distribution function cannot be chosen to describe all the Yushmanov particles; this is the reason why the use of variables ε and μ is advantageous. We also note that the distribution function is connected smoothly at the interface, which is indicated by arrows in Figs. 1 and 11.

5. Conclusions

We have described a relativistic, multiregion, bounce-averaged Fokker–Planck code, which was developed primarily to study the physics of mirror machines on a collisional time scale, including neutral beam injection, electron-cyclotron resonant heating, and synchrotron radiaion loss. The use of a Galerkin finite element method made it easier to implement the boundary conditions, especially at the interface of regions. The mapping technique was introduced to determine curved boundaries accurately and to improve the efficiency of the finite element procedure.

We have also presented the results of two example problems using the code; these examples show good agreement between our code, other Fokker–Planck codes, a Monte Carlo code, and analysis. Although the development of the code was motivated by the need to study present and future tandem mirror machines, the code is flexible enough to be used for other problems, including those in tokamaks (e.g., current drive [14] by lower-hybrid wave heating or ECRH).

Two major areas need to be improved or extended: one is a nonlinear relativistic collision operator; and the other is the self-consistent potential and finite-β effect. The fully nonlinear relativistic collision operator will be needed to study ECRH problems where hot electrons of several hundred keV in energy are involved as in MFTF-B [15]. Recently, Karney and Fisch [16] derived a Rosenbluth form for the collision operator for a weakly relativistic plasma. Their Fokker–Planck operator can be implemented in our code for an improved treatment of weakly relativistic electron–electron collisions. Including the self-consistent potential and finite-β effect in the code is a complex problem because the phase-space topology changes in time (i.e., the multivalued nature of the distribution function changes because of the appearance and disappearance of regions in the phase space). The extension of the code into these areas is currently in progress.

ACKNOWLEDGMENTS

We wish to thank L. D. Pearlstein and D. E. Baldwin for their numerous suggestions, enthusiastic support, and encouragement for this work. We are grateful to D. E. Fyfe and I. B. Bernstein for their unselfish assistance and suggestions, which were invaluable to us. Thanks are also due S. C. Eisenstat and M. H. Schultz for their advice and suggestions on the finite element method; T. D. Rognlien for helfpul discussions and the Monte Carlo code result; and M. E. Rensink for discussions on bounce-averaged Fokker–Planck codes. This work was performed under the auspices of the U.S. Department of Energy by the Lawrence Livermore National Laboratory under Contract W-7405-ENG-48.

REFERENCES

1. J. KILLEEN AND K. D. MARX, *Methods in Computational Physics* (Academic Press, New York, 1970), Vol. 9, p. 421.
2. J. KILLEEN, A. A. MIRIN, AND M. E. RENSINK, *Methods in Computational Physics* (Academic Press, New York, 1976), Vol. 16, p. 389.
3. T. A. CUTLER, L. D. PEARLSTEIN, AND M. E. RENSINK, "Computation of the Bounce-Average Code," Lawrence Livermore National Laboratory, Livermore, CA, UCRL-52233, 1977 (unpublished).
4. D. E. FYFE AND I. B. BERNSTEIN, *Nucl. Fusion* **21**, 1581 (1981).
5. G. D. KERBEL AND M. G. MCCOY, "Kinetic Theory and Simulation of Multispecies Plasmas in Tokamaks Excited with ICRF Microwaves," Lawrence Livermore National Laboratory, Livermore, CA, UCRL-92062, 1985 (unpublished).
6. D. E. BALDWIN AND B. G. LOGAN, *Phys. Rev. Lett.* **43**, 1318 (1979).
7. I. B. BERNSTEIN AND D. C. BAXTER, *Phys. Fluids* **24**, 108 (1981).
8. D. E. FYFE, A. WEISER, I. BERNSTEIN, S. EISENSTAT, AND M. SCHULTZ, *J. Comput. Phys.* **42**, 327 (1981).
9. C. DEBOOR, *A Practical Guide to Splines* (Springer–Verlag, New York, 1978).
10. S. C. EISENSTAT, M. C. GURSKY, M. H. SCHULTZ, AND A. H. SHERMAN, Yale University, New Haven, CT, Department of Computer Science Research Report 114 (unpublished).
11. T. C. SIMONEN, S. L. ALLEN, T. A. CASPER, J. F. CLAUSER, C. A. CLOWER, F. H. COENSGEN, D. L. CORRELL, W. C. CUMMINS, C. C. DAMM, M. FLAMMER, J. H. FOOTE, R. K. GOODMAN, D. P. GRUBB, E. B. HOOPER, R. S. HORNADY, A. L. HUNT, R. G. KERR, A. W. MOLVIK, R. H. MUNGER, W. E. NEXSEN, T. J. ORZECHOWSKI, W. L. PICKLES, P. PAULSEN, M. E. RENSINK, B. W. STALLARD, W. C. TURNER, W. L. HSU, W. BAUER, T. L. YU, AND D. ZIMMERMANN, *Phys. Rev. Lett.* **50**, 1668 (1983).
12. Y. MATSUDA AND T. D. ROGNLIEN, *Phys. Fluids* **26**, 2778 (1983).
13. R. H. COHEN, *Phys. Fluids* **26**, 2774 (1983).
14. C. F. F. KARNEY AND N. J. FISCH, *Phys. Fluids* **22**, 1817 (1979).
15. *Physics Basis for an Axicell Design for the End Plugs of* MFTF-B, edited by D. E. Baldwin and B. G. Logan (Lawrence Livermore National Laboratory, Livermore, CA, 1982), UCID-19359.
16. C. F. F. KARNEY AND N. J. FISCH, *Phys. Fluids* **28**, 116 (1985).